Forest destruction and its impact on land surface temperature using satellite data (Case Study: Forests of Hiran Region)

Jafar Jafarzadeh[1]*, A.A. Kakroodi [2], Yousef Erfanifard [3]

[1]*Faculty of Geography, Remote Sensing and GIS Department, University of Tehran, Tehran, I.R. Iran*
[2]*Faculty of Geography, Remote Sensing and GIS Department, University of Tehran, Tehran, I.R. Iran*
[3]*Faculty of Geography, Remote Sensing and GIS Department, University of Tehran, Tehran, I.R. Iran*

ABSTRACT

Forests play a crucial role in the context of climate change. In order to comprehensively grasp and improve our ability to predict the interplay between forest biodiversity, ecosystem functioning, and weather patterns affected by climate change, continuous monitoring of forests is imperative to track and mitigate destruction and degradation. In this research, satellite image processing was employed to monitor the impact of forest destruction on the microclimate of the region and its subsequent effect on surface temperature. The study collected data from 60 land points, consisting of 30 areas with trees and 30 treeless pasture areas. Next, the normalized differential vegetation index (NDVI) was utilized to distinguish between tree and non-tree areas. Subsequently, the surface temperature of the studied area was calculated using the single-channel method. Finally, a comparison was made between a selected study region and a control region to evaluate the impact of global warming, and statistical analysis was performed. The results of the classification of the region based on tree and non-tree areas showed that between 1984 and 2021, approximately 1,400 hectares were deforested .Additionally, the results of the final Welch's t-test statistical analysis demonstrated a significant difference between the temperatures of the two regions with a confidence level of 99% and a p-value of 0.0007. This fact underscores the significant impact of deforestation on the rise in regional temperatures.

1. Introduction

A forest is a vast expanse filled with trees, shrubs, and various other organisms that coexist and play a vital role in the Earth's ecosystem. Its primary function is to absorb carbon dioxide and produce oxygen through the process of photosynthesis, thereby maintaining the environmental balance (Ya'acob et al., 2012). However, deforestation stands as a major factor contributing to the decline of global biodiversity and acts as a significant source of carbon emissions (Higginbottom et al., 2019). Deforestation also leads to climate change, habitat loss, and various other detrimental effects (Kim, 2010). As human populations continue to grow, challenges arise from increased population density, urban expansion encroaching on wildlife habitats, and changes in land use patterns that conflict with

social and environmental conservation efforts. These problems are further exacerbated by changes in weather patterns (Behzadi & Mousavi, 2019).

Over the past few decades, the Caspian forests have experienced significant human interference. The easy accessibility, abundance, and diversity of valuable forest products have resulted in increased population density, the establishment of new residential areas, and extensive deforestation activities (Hashemi et al., 2016). Achieving sustainable forest management necessitates a wealth of information regarding various forest variables. However, gathering such extensive information using traditional methods, especially in large areas, can be costly, time-consuming, and labor-intensive. Moreover, given the rapid changes occurring in nature, there is a need for repeated and short-term estimations (Ahamed et al., 2011; Stehman,

2004). Deforestation stands as one of the most significant global environmental problems, posing a major threat to biodiversity and being a key driver of land use change. The average global forest area per capita is estimated to be 0.6 hectares. Approximately 14.2% of the world's forests are located in the vast continent of Asia. On average, it can be said that the per capita forest area in Asia is around 0.2 hectares (*Bruvoll et al., 2003;* *Dobson et al., 1997;* *Sodhi et al., 2004*). Deforestation stands as one of the primary drivers of land use changes and has been identified as the greatest threat to global biodiversity. In recent decades, remote sensing data have been extensively employed to obtain land use/land cover information, including changes such as forest reduction, urbanization rates, agricultural intensification, and other human-induced transformations (*Alrababah & Alhamad, 2006*). Satellite imagery has played a crucial role in classification processes, particularly in creating user or land cover maps and detecting land cover conditions (*Lobo et al., 2004;* *Nazmfar & Jafarzadeh, 2018*). The forests in the northern regions of Iran, which hold significant value, have experienced changes and conversions for various reasons in recent years. Recognizing the location and assessing the extent of forest changes in any region can greatly contribute to understanding their historical condition and aid in planning for their restoration (*Ghanbari & Shatai, 2010*). One of the ways to prepare vegetation and land use maps is by using satellite data and the image classification process (*Feizizadeh et al., 2018;* *Jafarzadeh & Nazmfar, 2019*). The northwest regions of the country have their own climatic characteristics. Air masses entering this region from the northwest, west, and north bring snow and rain during spring and winter (*Jafarzadeh, 2022*). *Zeng et al. (2021)* investigated the warming caused by deforestation in tropical mountainous regions, which varies with altitude. Their research found that local temperature anomalies caused by extensive deforestation can reach up to 2 degrees Celsius. *He et al. (2015)* conducted a study on the change in energy budget observed through satellite data due to deforestation in Northeast China and its climatic consequences. They evaluated the potential changes in the energy budget by quantifying differences in MODIS images of surface physical characteristics between cropland and forest. *De Frenne et al. (2021)* reviewed the importance, drivers, and future research agenda of forest microclimates and climate change. They investigated how spatial and temporal changes in forest microclimates are influenced by forest characteristics, local water balance, topography, geography, and landscape composition. *Chen et al. (2017)* studied the effects of climate on soil carbon processes along an altitudinal gradient in the Lukillo tropical forest. They conducted a soil displacement experiment along an altitude gradient, with decreasing temperature and increasing humidity, to examine the effects of climate change on soil organic carbon (SOC) and soil respiration. Their results showed that soil carbon and respiration rates were both affected by microclimate changes. Soils transferred from low to high altitudes exhibited increased respiration rates, along with decreasing SOC content at the end of the experiment, indicating that increased soil moisture and altered soil microbes may affect respiration rates. *Cinoğlu et al. (2021)* investigated the climatic landforms resulting from post-fire interactions between Ceanothus species and Douglas-fir in the Klamath Mountains (California). They sampled post-fire vegetation and soil biogeochemistry in 57 plots along a time gradient from the time of the fire (7-28 years) and climatic water deficit (dryness). The results of their work showed that Ceanothus biomass increased while Douglas-fir biomass decreased with increasing dryness. High aridity and Ceanothus biomass interacted to affect soil C:N more than either factor alone. *Hofmeister et al. (2021)* examined the effect of microclimate edges in small patches of temperate forests in the context of climate change. They demonstrated that the thermal gradient from the forest edge to the forest interior deserves special attention due to the observed increase in ambient air temperature over the past decades, although the edge effect may be a combination of various environmental conditions. They concluded that the edge effect could be mitigated to some extent by preventing further forest fragmentation and adopting wood harvesting methods that avoid excessive clearing, such as single tree selection. *Ghanbari and Shatai (2010)* investigated changes in forest cover using aerial photos and Esther images, focusing on marginal forests in the south and southwest of Gorgan city. The study evaluated changes in forest cover over three time periods (1966-1995-2007) using satellite images and aerial photographs. The results revealed significant forest area conversion to non-forest lands during the 41-year period. The annual change rate of natural forests was higher during the period of 1966-1995 compared to 1995-2007. *Nasirnia & Esmaeili (2008)* investigated deforestation in Iran and neighboring countries using the Kuznets model. The results of this study, like previous studies conducted in the Asian region, rejected the hypothesis of the existence of the Kuznets environmental curve for the selected countries. The only variable found to significantly affect the deforestation process in this study was the population variable. The lack of significance of the institutional variable indicates that the selected countries are homogeneous based on the selected index. *Hashemi et al. (2016)* investigated the monitoring of forest cover changes in the SiahMezgi basin of Gilan province using Landsat images. The results showed a decrease in the area of forest land by 213.55 hectares between 2000 and 2015. *Mahmoudzadeh & Azizmoradi (2019)* conducted a study on deforestation modeling using a neural network and geographic information system in forests around Khorramabad. The results of the network test,

involving all variables, indicated an appropriate accuracy of the modeling obtained from the multilayer perceptron, with a mean squared error value of 0.13. Additionally, using the receiver operating characteristic (ROC) curve, the multilayer perceptron model exhibited high accuracy, with an area under the curve equal to 0.88, when comparing the actual values of deforestation against the resulting model.

In this research, the aim is to utilize Landsat satellite image processing to calculate surface temperature and extract tree density in the Hiran forests, located on the border of Gilan and Ardabil provinces, as well as the border of the Republic of Azerbaijan. The normalized difference vegetation index (NDVI) is employed to examine the correlation between deforestation, tree destruction in the region, and heat stress. This study is the first of its kind in the region and stands out for its use of precise ground control points and statistical calculations to ensure result accuracy. Through statistical analysis and various statistical tests, the final outcomes will reveal the relationship between deforestation and temperature (Jafarzadeh et al., 2023). Innovation in this research could be:

1.Utilizing satellite data: The use of satellite data to investigate the impact of forest destruction on land surface temperature in the Hiran region is a novel and advanced approach. Satellite data can provide accurate information about temperature changes over time and in large areas.

2.The impact of forest destruction on land surface temperature: Researching the impact of forest destruction on land surface temperature can help us gain a better understanding of the relationship between forest

destruction and temperature changes in the study area. This research can introduce methods and solutions for proper forest management and this reduction of deforestation.

3.Case study of the Hiran region: Choosing the Hiran region as a case study allows us to analyze the impact of forest destruction on land surface temperature in a more detailed and comprehensive manner. This selection can help us have a better awareness of desertification and climate changes in this area and provide suitable strategies for preserving forests and controlling temperature changes.

4.Providing management solutions: This research can offer management strategies and solutions for reducing forest destruction and controlling temperature changes. These solutions can include reforestation programs, sustainable logging practices, conservation efforts, and policies to promote forest preservation.

2. Materials and Methods

2.1. Area of Study

The research focuses on an area of 47,590 hectares situated in the northern region of the Islamic Republic of Iran. This

area spans across the provinces of Gilan and Ardabil, as well as parts of the border with the Republic of Azerbaijan, and is recognized as one of Iran's forested regions (Imani et al., 2020). These forests are part of the Hyrcanian forests. The study area stretches from 48.33 degrees to 48.50 degrees east longitude and 38.23-38.26 degrees north latitude. In total, Iran's forests encompass approximately 3,400,000 hectares along the northern slopes of the Alborz Mountains and the coastal provinces of the Caspian Sea. Additional scattered forests cover up to three million hectares in other parts of the country. Figure 1 illustrates the delineated study area.
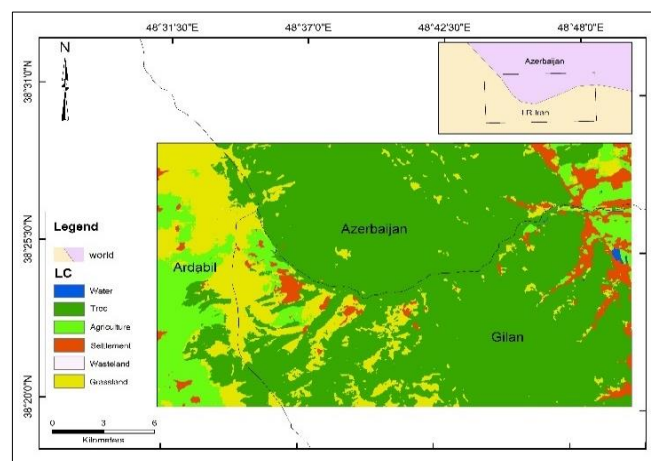
(a)

(b)

Figure 1. (a) The map of the study area, (b)The Google Earth scheme

2.2. Data Used

In this research, satellite data from Landsat 4, 5, and 8 for the years 1984, 1994, 2005, 2014, and 2021 were utilized (see Appendix 1). The land use classification image derived from the Sentinel 2 satellite was also employed to delineate the study area (Jafarzadeh & Attarchi, 2023). The data processing and analysis were conducted using ArcGIS software version 8.10 and ENVI satellite image processing software version 5.3. Additionally, RStudio programming software was employed for the statistical analysis of the research. Figure 2 provides a schematic representation of
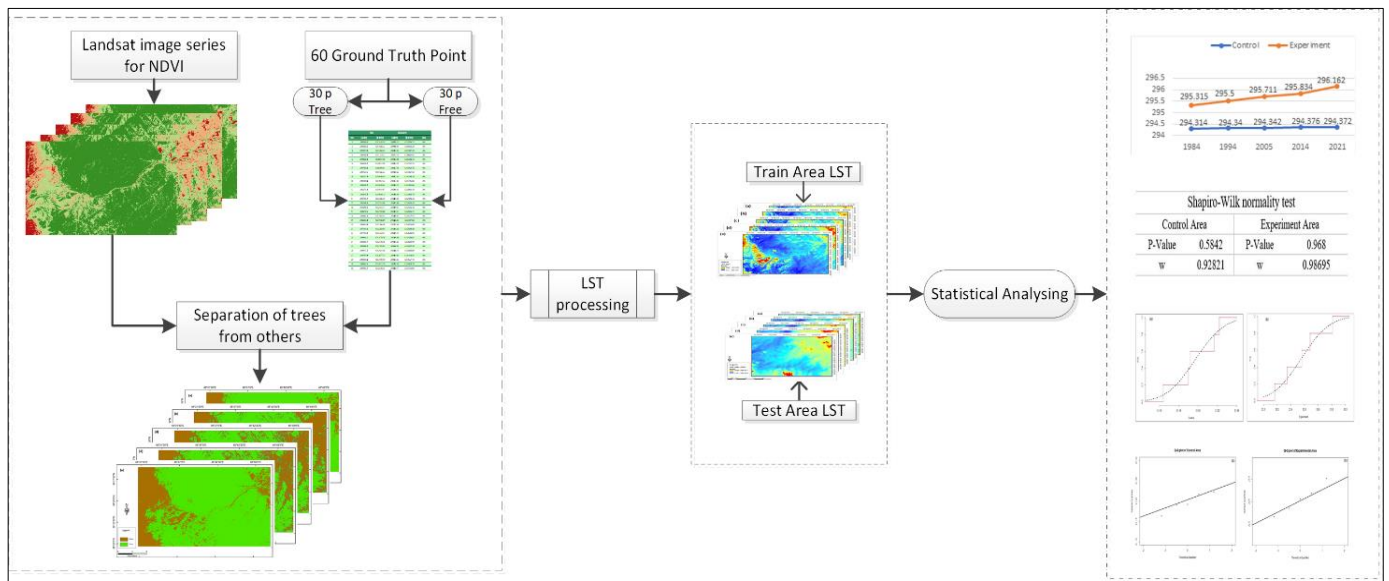
the research methodology and steps.

Figure **2**. *Process of research*

The steps involved in conducting this method are as follows: 1) Satellite data collection: In this stage, the required satellite data for investigating land surface temperature and forest destruction is collected. This includes high-resolution satellite images and land surface temperature data captured at different time intervals. 2) Satellite data processing: During this stage, satellite data is processed to obtain more accurate information regarding land surface temperature and forest destruction in the Hiran region. This involves image correction and extraction of temperature parameters and forest characteristics. 3) Data analysis: In this phase, the processed data is analysed. Examining the temporal variations in land surface temperature and its correlation with forest destruction is one of the main objectives. Patterns and trends related to temperature changes and forest destruction can be analysed to understand their respective roles in land surface temperature changes. 4) Comparison with reference areas: For a comprehensive assessment of the impact of forest destruction on land surface temperature, the results can be compared with reference areas or regions that have preserved forests. This comparison helps in identifying the specific influence of forest destruction on land surface temperature.

By following these steps, the research aims to provide valuable insights into the relationship between forest destruction and land surface temperature, specifically in the Hiran region. The selection of specific dates, such as 1984, 1994, 2005, 2014, and 2021, for analyzing the effect of deforestation on land surface temperature (LST) is based on several criteria. These criteria may vary depending on the research objectives and available data. Here are some

common reasons for choosing these specific dates:

1. Baseline Comparison: The initial reference date, such as 1984, provides a baseline to compare the subsequent years and assess the changes in forest cover and LST over time. By comparing LST values across multiple years, the researchers can identify temporal trends and analyze the impact of deforestation on land surface temperature.

2. Availability of Satellite Data: The availability of satellite imagery for the selected dates is a crucial factor. Researchers typically choose dates for which high-quality and consistent satellite data are readily accessible. For instance, the Landsat series of satellites, which provide multispectral data suitable for land cover analysis, have data available for multiple time points, including 1984, 1994, 2005, 2014, and 2021.

3. Long-Term Trends: The selected dates span a considerable time range, allowing researchers to observe and analyze long-term trends in deforestation and its effects on LST. By including both earlier and more recent dates, the study can capture changes over several decades and provide a comprehensive understanding of temporal patterns.

2.3. *Normalized Difference Vegetation Index (NDVI)*

The Normalized Difference Vegetation Index (NDVI) is a widely used graphical index in remote sensing analysis for evaluating vegetation presence and density in a given area. It serves various purposes such as studying vegetation dynamics over time, climate modelling, global vegetation classification, monitoring agricultural productivity, assessing desertification and drought, environmental conservation, and assessing global energy and water balance. The NDVI values range between +1 and -1, indicating the extent of vegetation cover. The calculation of the NDVI index follows Equation 1 (*Gates, 1980*):

$$NDVI = \frac{(NIR - RED)}{(NIR + RED)} \qquad (1)$$

Where: NIR=Near Infra-Red Band and RED= Red Band

2.4. Calculation of LST

Every object with a temperature above absolute zero emits thermal radiation, including the Earth's surface (Alavi-Panah, 2008). The surface temperature of the Earth is a crucial parameter in the field of Earth sciences. It is influenced by various factors such as incoming solar radiation, surface emissivity, humidity, and atmospheric circulation. Understanding the surface energy balance and accurately measuring surface temperature are essential for studying climate patterns, predicting natural disasters, managing water resources, and conducting other Earth sciences research (Jafarzadeh & Hasanitabar, 2021).

2.5. Single channel method

In the single-channel method, LST is calculated through equation (2) (Isaya & Avdan, 2016):

$$T_s = \gamma \left[\varepsilon^{-1} \left(\psi_1 \backslash times L_{sensor} + \psi_2 \right) + \psi_3 \right] + \delta \qquad 2)$$

Where   Ts=LST

T_{sensor} = sensor brightness temperature in Kelvin

γ = effective wavelength of a thermal infrared band

ψ = atmospheric effect modifier on

L_{sensor} = thermal radiance

δ, a parameter that depends on the Planck function and γ is the wavelength at which the detector works and are calculated through relations (3 to 7) (Cristóbal et al. 2018):

$$\psi_1 = 0.04019\omega^2 + 0.02916\omega + 1.01523 \qquad (3)$$

$$\psi_2 = -0.38333\omega^2 - 1.50294\omega + 0.20324 \qquad (4)$$

$$\psi_3 = 0.00918\omega^2 + 1.36072\omega - 0.27514 + 1.0152 \qquad (5)$$

$$\gamma = L_{sensor} - T_{sensor}^2 / b_\gamma \qquad (6)$$

$$\delta = T_{sensor}^2 / b_\gamma \times L_{sensor} \qquad (7)$$

In these relationships, L_{sensor} is the radiance of the thermal band, T_{sensor}^2 is the temperature of the radiance of the thermal band, and both parameters were calculated for band 10. b_γ is a constant number that is equal to 1324K for band 10 (Vandegriend et al., 1992). To perform the steps of the single-channel algorithm for calculating the earth's surface temperature, we first calculate the Radiance of Landsat thermal band 10 number 1. All steps are done inside the ENVI5.3.1 software. After calculating the brightness temperature of band 10, the next step is to calculate the emissivity of the Landsat image. The process of calculating

emissivity involves separate steps that are introduced in a specific order. Here is a breakdown of these steps:

1. Perform atmospheric correction of the multi-spectral bands, which include the blue, green, red, and infrared bands. This correction is achieved using the QUAC (QUick Atmospheric Correction) command within the software. It helps to account for atmospheric effects on the image data.

2. Convert the resulting image into decimal values since the initial values are integers. This conversion is done by dividing all the pixel values of the image by 10000.0. The purpose of this step is to obtain reflectance values for the image.

3. Calculate the Normalized Difference Vegetation Index (NDVI) using the band calculation tool available in the software. NDVI is a vegetation index that helps assess the presence and health of vegetation based on the contrast between near-infrared and red spectral bands.

4. Implement the calculation algorithm proposed by Zhang et al. (2006) to calculate the emissivity. This algorithm takes into account the NDVI values and specific conditions for emissivity calculation. These conditions are applied within the software using the provided tools and options.

5. Obtain the emissivity image as the final result of the calculations. The emissivity image represents the estimated emissivity values for different areas in the Landsat image, which are crucial for further analysis and interpretation.

By following these steps, the brightness temperature, reflectance, NDVI, and emissivity of the Landsat image can be calculated and utilized for various applications and studies. The conditions introduced by Zhang et al. are shown in Table 1:

Table 1. Emissivity calculation conditions are based on the NDVI index (Zhang et al., **2006**)

NDVI	LSE
NDVI < -0.185	0.995
-0.185 ≤ NDVI < 0.157	0.985
0.157 ≤ NDVI ≤ 0.727	1.009 + 0.047 - ln (NDVI)
NDVI > 0.727	0.990

to introduce these conditions to the software, we enter the following values in the band calculation menu:

Emissivity=(b1 lt (-0.185))*0.995 + (b1 ge (-0.185) and b1 lt 0.157)*0.985 + (b1 ge 0.157 and b1 le 0.727)*(1.009 + 0.047 * (alog(b1))) + (b1 gt 0.727)* 0.990

To calculate the amount of γ, we use equation 8 (Cristóbal et al. 2018):

$$\gamma = \left\{ \frac{C_2 L_{sensor,\lambda}}{T_{sensor}^2} \left[\frac{\lambda^4}{C_1} L_{sensor,\lambda} + \lambda^{-1} \right] \right\}^{-1}$$

(8)

Where C1 and C2 = coefficients of atmospheric parameters and λ= wavelength.

To calculate the amount of gamma using the software, we use the following expression in band calculations:

given in equation 6. To calculate the amount of δ in the software, we use the following relationship (9):

$$Delta = (-b1) * b2 + b3 \qquad (9)$$

In this relationship, b1 is equivalent to the gamma value, b2 is equivalent to the radiance image and b3 is equivalent to the brightness image.

The next step is to calculate ψ values using relations 10, 11, and 12:

$$\psi_1 = 0.14714\omega^2 - 0.15583\omega + 1.1234 \qquad (10)$$

$$\psi_2 = -1.1836\omega^2 - 0.3760\omega - 0.52894 \qquad (11)$$

$$\psi_3 = -0.04554\omega^2 + 1.8719\omega - 0.39071 \qquad (12)$$

To calculate these values, we must first calculate the value of ω. This value is obtained using equation 13 ([Liu & Zhang, 2011](#); [Rongali et al., 2018](#)):

$$\omega_i = 0.0981 \times \left\{ 10 \times 0.6108 \setminus timesexp\left[\frac{17.27 \times \left(T_0 - 273.15\right)}{237.3 + \left(T_0 - 273.15\right)} \right] \setminus timesRH \right\}$$

$$+ 0.1679$$

$$(13)$$

In this regard, we must have the relative humidity and temperature of the station at the time of taking the image. To obtain these values, we use the report of the synoptic station of the studied area. We can also use https://www.ogimet.com/to get these values.

2.6. Shapiro-Wilk test

The Shapiro-Wilk test is a statistical test used to determine if a dataset follows a normal distribution. It is part of the group of non-parametric statistical methods and helps assess the normality of data. The test relies on the statistic produced and the associated probability value (P-value) generated by most statistical software. In the Shapiro-Wilk test, the estimation of distribution parameters is not considered in its original form. Instead, it uses ordinal statistics and their distribution along with the original data. Due to this characteristic, it is classified as a non-parametric method. To determine whether to reject the null hypothesis, which assumes that the data is sampled from a normal population, we examine the significance value (Sig). If the Sig value is less than 0.05 (typically chosen as the threshold), we reject the null hypothesis and conclude that the sample data does not follow a normal distribution. By conducting the Shapiro-Wilk test and interpreting its results, researchers can gain insights into the distributional characteristics of their data

Gamma=1/ (((14387.7 * b1)/(b2^2.0)) * (((10.4 ^ 4.0)/ (1.19104 * (10 ^ 8.0))) * b1 + (1/ 10.9)))

Then the next step is to calculate the value of δ which was

and make informed decisions regarding the use of appropriate statistical methods and assumptions. Equation 14 shows the test statistic:

$$W = \frac{\left(\sum_{i=1}^{n} a_i x_{(i)} \right)^2}{\sum_{i=1}^{n} \left(x_i - \bar{x} \right)^2} \qquad (14)$$

$\bar{x}$ means the mean of observed values from a random sample.

2.7. t-test with two independent samples

This test compares the averages of two groups of respondents. In other words, it assesses the averages obtained from random samples. This means that we randomly select samples from two different communities, regardless of whether the number of samples is equal or unequal, and compare the averages of those two communities. This method is based on the normal t-distribution and is most effective for small samples when the variable data being compared in independent groups follows a normal distribution. The average comparison test of two independent populations is one of the most commonly used tests in statistical analysis. It allows us to compare the averages of two independent societies and determine their statistical difference. When the data from the communities follow a normal distribution, the t-test and its statistic are suitable for comparing the means of the two communities. However, when this distribution is not clear, it is better to use similar non-parametric tests such as the "Mann-Whitney test". Equation 15 presents the statistics of this test ([McElduff, 2010](#)).

$$t_{obt} = \frac{\bar{x} - \mu}{S_{\bar{x}}} \qquad (15)$$

2.8. T-welch test

This test, similar to the two-sample t-test, is used to compare the averages of two populations. In Welch's t-test, it is assumed that the variances of the two populations are not equal ([Welch, 1947](#)).

۲.۹. Leven test

One of the inferential statistics used to assess the equality of variances among multiple independent populations is Levene's statistic, which is employed in a test known as "Levene's test." In most statistical software, the calculation and execution of this test are provided as a prerequisite for other tests. For instance, when examining the equality of means between two independent populations, the assumption

of equal or unequal variances will yield separate statistics with different degrees of freedom for the mean test. The null hypothesis in Levene's test posits the equality of variances. Thus, if σ_1^2 and σ_2^2 represent the variances of two independent populations, the null hypothesis for this test can be expressed as equation 16 ([Schultz, 1985](#)):

$$\begin{cases} H_0: & \sigma_1^2 = \sigma_2^2 \\ H_1: & \sigma_1^2 \neq \sigma_2^2 \end{cases} \qquad (16)$$

Suppose we have sampled k independent groups or communities, and the observations obtained from these groups are denoted as Y_{ij}. If we define Z_{ij} as the deviation of the observations in group i from the group mean, represented by $\bar{Y}_i$, the Levene test statistic is calculated as equation 17:

$$W = \frac{(N-k)}{(k-1)} \frac{\sum_{i=1}^{k} N_i \left(Z_{i.} - Z_{..}\right)^2}{\sum_{i=1}^{k} \sum_{j=1}^{N_i} \left(Z_{ij} - Z_{i.}\right)^2} \qquad (17)$$

Additionally, it is important to note that the subscript of the group average should be denoted as $\bar{Y}$ and Z_i represents the average of the i-th group. It is evident that N refers to the total number of observations, while N_i specifically denotes the number of observations in group i. The Levene test statistic, denoted as W, follows an approximate F-distribution with degrees of freedom k-1 and N-k. Hence, the obtained value of the statistic W should be compared to the α-th quantile of the F-distribution with these degrees of freedom. If the calculated value of the statistic W (equation 18) exceeds the F-distribution quantile, the null hypothesis is rejected (Levene, 1960).

$$W > F\left(\alpha; k-1, N-k\right), \ \ Reject \ H_0 \qquad (18)$$

Usually, the value of α is considered equal to 0.05 or 0.01 ([Derrick, 2018](#)).

3. Results and discussion

Field data collection was conducted in the study area using a single-frequency handheld GPS device, specifically the Garmin 12 model. Land points were recorded, totalling 60 points, representing areas with tree cover as well as pasture and grass vegetation. The sampling process was carried out randomly, comprising 30 points from areas with tree cover and 30 points from vegetation areas of pasture and grass. These points were selected to align with the spatial resolution of the Landsat image, which is 30 meters. Care was taken to ensure that the selected points were spaced within distances less than thirty meters apart from each other the points related to tree vegetation encompass

areas with varying tree cover densities, including locations with dense and mature trees, as well as areas with sparse tree cover and young trees. The harvested points were imported into ENVI software and overlaid onto the study area to examine their spectral reflectance values and compare them with other points. By analyzing the differences between these points and determining a threshold value on the normalized vegetation index image, the image was subsequently reclassified into two classes using new values. The threshold values were determined by comparing the ground-based collected points with the satellite image and the normalized vegetation index image. This involved conducting an experimental analysis and calculating the average value based on the 30 collected points. Figure 3 illustrates the calculated vegetation indices for the study area from 1984 to 2021, presented as a ten-year time series.
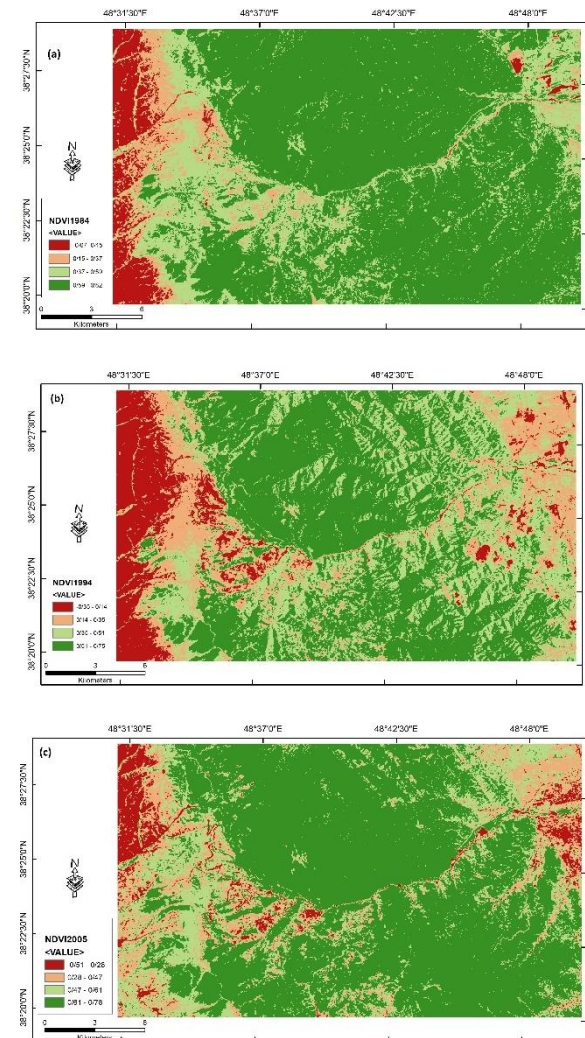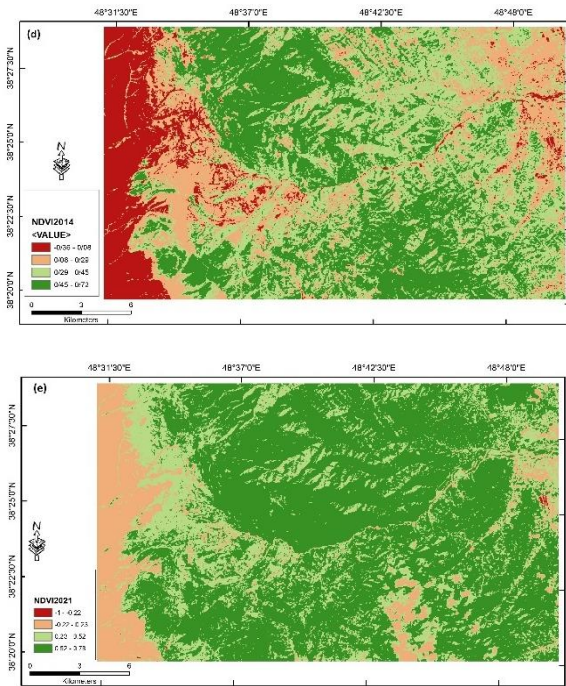
*Figure 3. Vegetation indicators were calculated for the study area during the years **1984** (a), **1994** (b), **2005** (c), **2014** (d), and **2021** (e)*

Figure 4 shows the separation of the tree layer from the pasture and others based on the analysis of the spectral graph of the pixels and the correspondence with the ground control point for 1984 to 2021. In this stage of the research, we employed the Normalized Difference Vegetation Index (NDVI) to relatively separate regions containing tree cover from other areas, including grasslands or herbaceous vegetation. To enhance the accuracy of tree separation from other existing vegetation cover in the study area, we utilized ground truth data collected from the study area using GPS devices. It is evident that achieving precise and comprehensive separation in this process is highly challenging, but the utilization of ground truth data has significantly improved the accuracy of the work to an acceptable level.
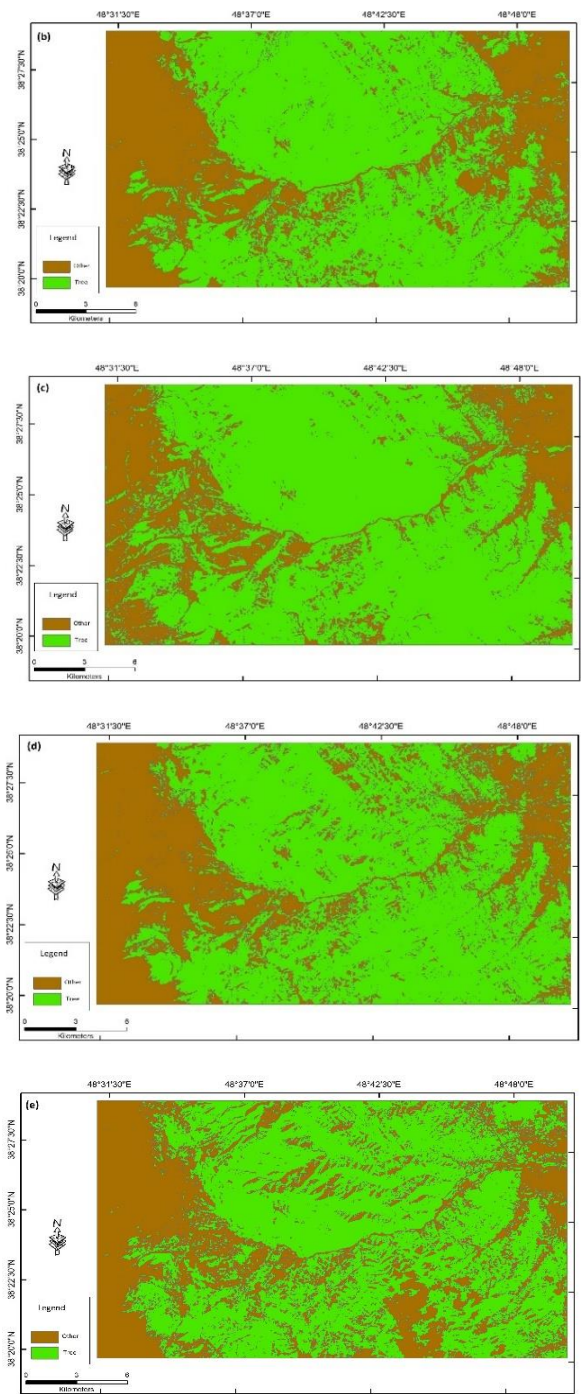
*Figure 4. Separation of tree class from pasture and others for **1984** (a), **1994** (b), **2005** (c), **2014** (d), and **2021** (e)*

Table 2 and Figure 5 provide an overview of the forest changes in the study area from 1984 to 2021. The data in the table reveals a decrease of approximately 2000 hectares in tree cover within the study area over the years. This decline can primarily be attributed to factors such as the construction of villas and housing, as well as the creation of communication pathways that necessitated the removal of trees. These observations were made during field visits conducted as part of the study. Figure 5 represents the decreasing trend of changes in the tree cover area in the study region, measured in hectares. As evident from the

graph, this trend unfortunately shows a declining pattern, with approximately 2000 hectares of trees lost over a period of about twenty years.

(b)

Year	Value (Hectar)	Tree Density
1984	40266	0.861
1994	40020	0.840
2005	39761	0.835
2014	39102	0.821
2021	38850	0.816

*Table **2**. Changes of trees in the study area from **1984** to **2021***

(c)
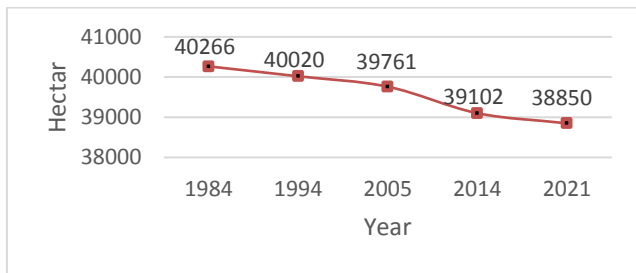
*Figure **5**. The diagram of forest changes from **1984** to **2021** in the study area (hectares)*

Figure 6 shows the calculated temperature map for the study area for the year (a) 1984, (b) 1994, (C) 2005, (d) 2014, and (e) 2021 in Kelvin.
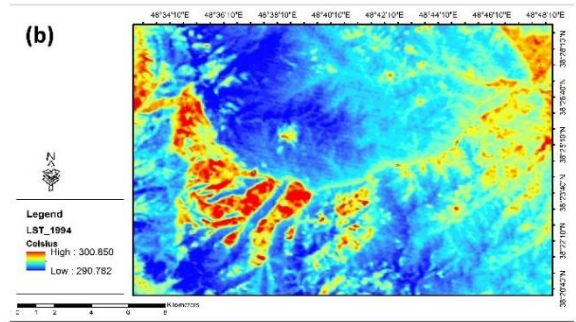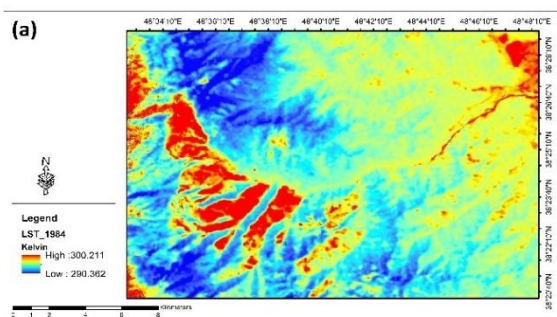

(d)

(a)

(e)
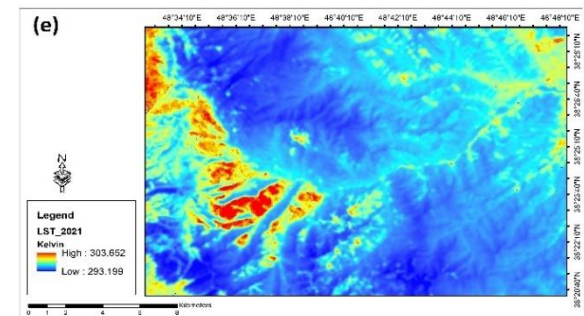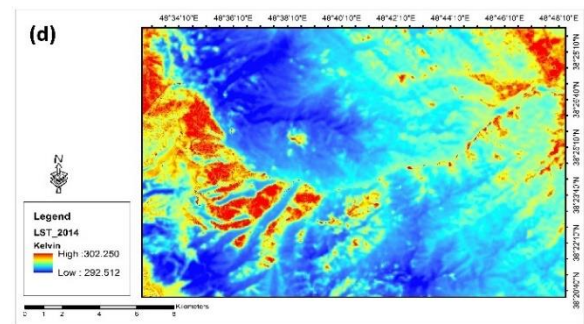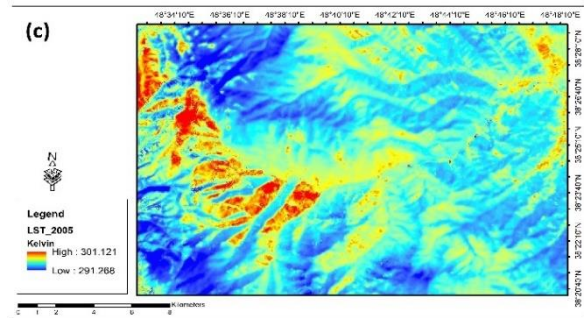
*Figure **6**. Land surface temperature in Kelvin for the years **1984**(a), **1994** (b), **2005** (c), **2014** (d), and **2021** (e)*

Table 3 presents the average changes in the earth's surface temperature for the years 1984 to 2021, expressed in Kelvin and degrees Celsius. The corresponding values are also depicted in Figure 7, which visually represents the average temperature changes. Based on the calculations, the temperature variation observed in the studied area between 1984 and 2021 amounts to 0.85 degrees Celsius.

*Table **3**. Calculated average temperature for the years **1984** to **2021** in Kelvin and degrees Celsius*
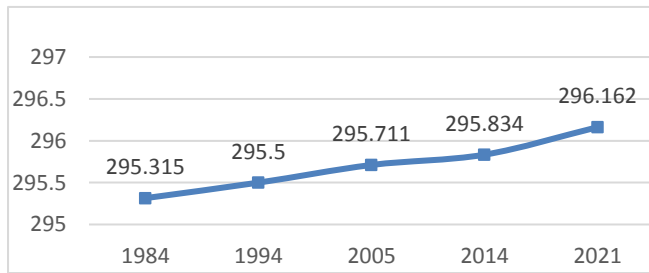

Figure 7. Temperature changes in the studied area in Kelvin

In the subsequent phase of the study, in order to distinguish and model the temperature changes specific to the study area from the overall global temperature changes, a nearby area is selected as a comparison area. This area should either have a similar size to the study area or have a proportional representation. The study area, for which the temperature has been calculated, is considered as the treatment or test area, while the new area is designated as the control area. This approach allows us to model the process of temperature changes and tree density. Additionally, the average temperature variations on the surface of the control area are also computed to further analyse the data. Figure 8 provides a visual representation of the location of the control area, which has an area one-tenth the size of the study area. The control area is selected within the study area in an area where minimal or no forest destruction has occurred, ensuring that the number of temperature changes during the study period and the ratio of global changes can be examined and compared.
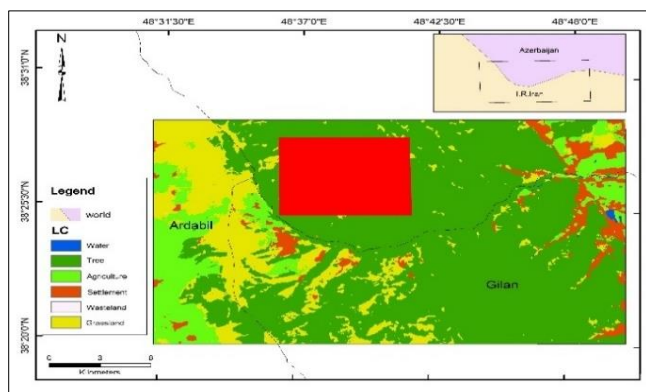

*Figure **8**. Control region for final modelling*

Table 4 presents the average surface temperature changes observed in the control area throughout the studied years.

Year	Kelvin	Celsius
1984	294.314	21.164
1994	294.340	21.190
2005	294.342	21.192
2014	294.367	21.217
2021	294.372	21.222

Additionally, Figure 9 provides a graphical representation, in Celsius units, of the average temperature changes recorded in the control area, corresponding to the data presented in Table 3.

*Table **4**. Calculated average temperature for the years **1984** to **2021** in Kelvin and degrees Celsius for the control area*

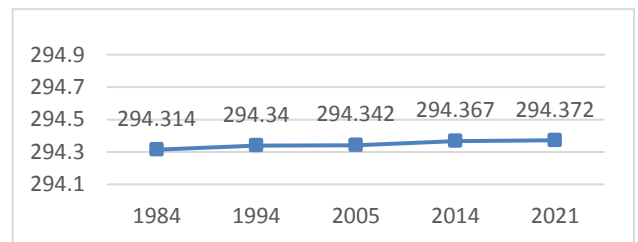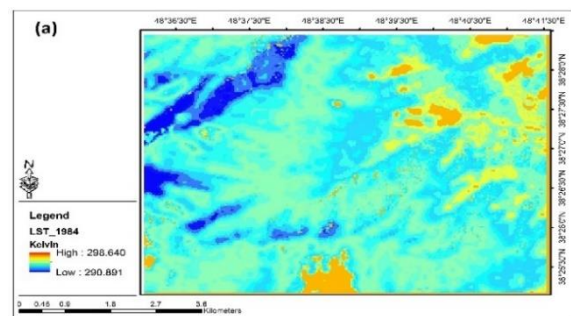| Year	Kelvin	Celsius
1984	295.315	22.165
1994	295.500	22.350
2005	295.711	22.561
2014	295.834	22.684
2021	296.162	23.012

*Figure **9**. Temperature changes in the control area in Kelvin*

Figure 10 shows the temperature calculated for the control area in Kelvin for the year (a) 1984, (b) 1994, (c) 2005, (d) 2014, and (e) 2021.

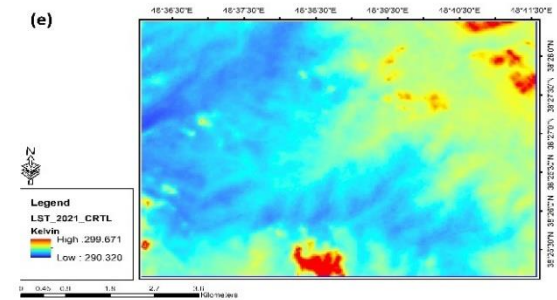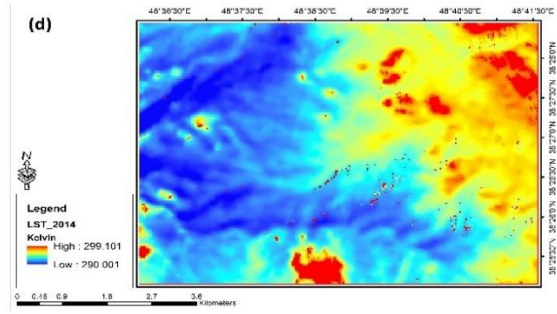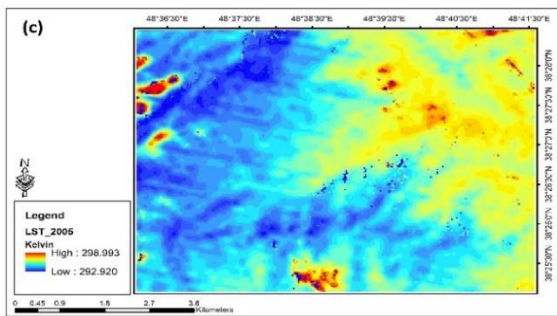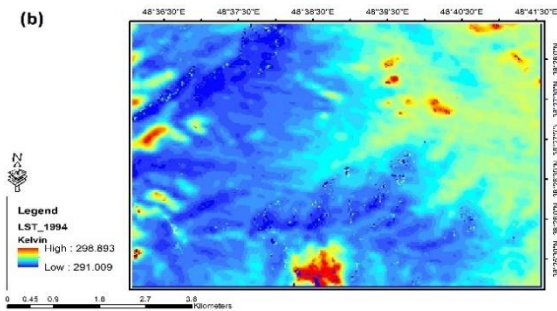|	Control Group		Experiment Group	
Year	Kelvin	Celsius	Kelvin	Celsius
1984	294.314	21.164	295.315	22.165
1994	294.340	21.190	295.500	22.350
2005	294.342	21.192	295.711	22.561
2014	294.376	21.217	295.834	22.648
2021	294.372	21.222	296.162	23.012

Figure 10. Calculated temperature for the area control in Kelvin for the years 1984(a), 1994 (b), 2005 (c), 2014 (d), and 2021 (e)

The authors acknowledged the global nature of temperature increase as a confounding variable and implemented a control group without deforestation or tree cutting to account for this factor. Statistical tests, including Shapiro-Wilk, independent t-test, Lune's test, and Welch's independent t-test, were conducted using RStudio programming software to compare the two regions. The results obtained from these tests are explained in Appendix 2. Table 5 presents the average temperature changes in both the control and test areas, expressed in Kelvin and degrees Celsius, for the period between 1984 and 2021. Additionally, Figure 11 visually represents the average temperature changes in both areas, using Celsius units, as depicted in the table.

Table 5. The average temperature changes of the control and test areas in terms of Kelvin and degrees Celsius from 1984 to 2021
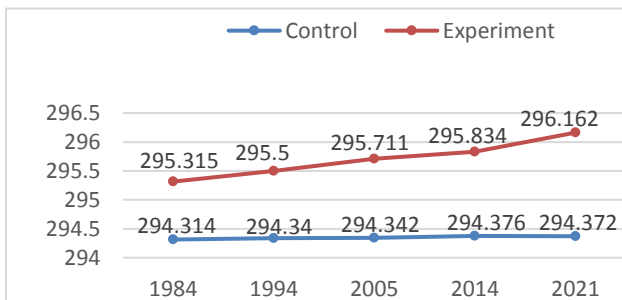

Figure 11. The average temperature changes of the control and test areas in Kelvin from 1984 to 2021

The Shapiro-Wilk test results indicated that the temperature data in degrees Celsius for both the control areas (p-value = 0.5842) and the experimental area (p-value = 0.968) followed a normal distribution. These findings are presented in Table 6. To visually assess the normality of the data, Figure 12 displays the Q-Q plot, which compares the observed data quantiles against the quantiles of a theoretical

normal distribution. Additionally, for a better understanding of the data distribution, Figure 13 depicts a curve diagram illustrating the empirical data distribution function overlaid on the theoretical normal distribution function.

*Table **6**. Shapiro-Wilk test results*

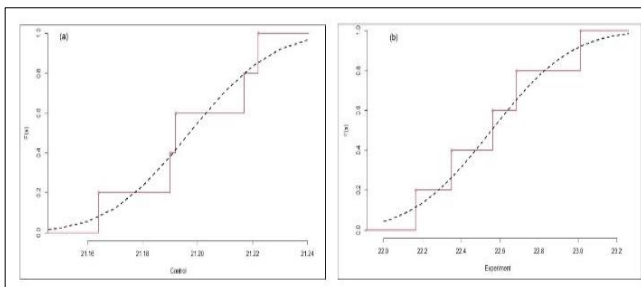| Shapiro-Wilk normality test			
Control Area		Experiment Area	
P-Value	۰,۵۸۴۲	P-Value	۰,۹۶۸
w	۰,۹۲۸۲۱	w	۰,۹۸۶۹۵
Shapiro-Wilk normality test			
Control Area		Experiment Area	
P-Value	۰,۵۸۴۲	P-Value	۰,۹۶۸
w	۰,۹۲۸۲۱	w	۰,۹۸۶۹۵

*Figure **12**. Q-Q plot to show the normality of the data of (a) control region and (b) test region*
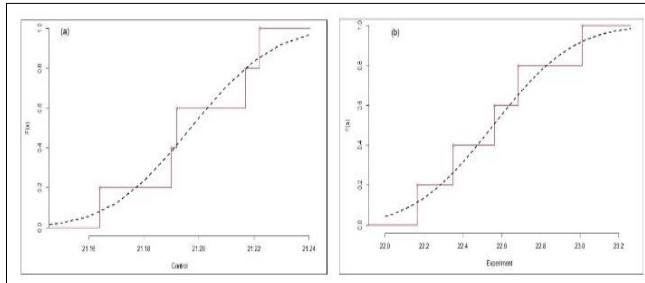

*Figure **13**. Experimental plot to show the normality of the data of (a) control area and (b) test area*

Given that the temperature data for both the control and experimental regions exhibited a normal distribution according to the Shapiro-Wilk test, the independent T-test was employed to assess the equality of average temperatures between the two regions. Prior to conducting the T-test, Levene's test was applied to examine the equality of variances between the two groups. The results of Levene's test rejected the hypothesis of equal variances at a 95% confidence level, indicating significant variance differences (p-value = 0.03145). Consequently, due to the unequal variances, the Welch's T-test was employed. This test, at a high level of significance (99%), rejected the null hypothesis of equal temperatures between the control areas and the experimental area (p-value = 0.0006944). The presence of uncertainty in the discussion and results section of a research study is a common occurrence and is typically

acknowledged by researchers. Uncertainty arises due to various factors, including limitations in data, methodology, and the complexity of the studied phenomena. Here are some reasons for the presence of uncertainty and the omission of certain factors in the analysis:1) Study Focus and Scope: Research studies often have specific objectives and limitations in terms of scope and available resources. While the selected study may focus on the impact of deforestation on land surface temperature, it might not account for all possible influencing factors due to constraints in data availability or the scope of the research. Uncertainty arises when factors outside the study's scope are not explicitly considered. 2) Data Limitations: The availability and quality of data can introduce uncertainties. In the case of surface temperature analysis, factors such as sensor limitations, atmospheric conditions, and data gaps can affect the accuracy and precision of the results. Researchers typically acknowledge these limitations and discuss the potential impact on the findings. 3) Complexity of Factors: Surface temperature changes are influenced by a multitude of factors, including land cover, topography, vegetation, urbanization, and atmospheric conditions. It may not be feasible to incorporate all these factors into a single study or to isolate their individual contributions effectively. Thus, the focus is often placed on the primary factor of interest (in this case, deforestation), while acknowledging that other factors may also contribute to the observed surface temperature changes. 4) Further Research and Recommendations: Recognizing uncertainties provides opportunities for further research and investigation. Researchers may suggest future studies to address the limitations and uncertainties identified in the current research. They may also recommend the inclusion of additional factors or the utilization of advanced methodologies to improve the understanding of surface temperature changes. Mahmoudzadeh & Azizmoradi (2019) analyzed deforestation changes using satellite images and found a significant reduction in forest area. A multilayer perceptron model accurately predicted deforestation trends, highlighting its effectiveness in understanding and predicting deforestation patterns which is consistent with the results of this research. According to this research and past researches in this field, it can be said that social factors have had the greatest impact on forest destruction; Among them, we can mention the increase in population, the expansion of cities, roads, and agricultural lands; which is consistent with the research results of Singh et al (2017) and Bonilla-Badoya et al (2018).

4. Conclusion

Deforestation has emerged as a detrimental outcome of human activities, leading to the destruction of forested areas worldwide. In recent years, the forests in northern Iran, known for their significant ecological value, have undergone

substantial transformations due to various human factors, such as the construction of residential villas and roads. This research aims to investigate the impact of deforestation on the microclimate of the region, particularly focusing on the surface temperature changes. To achieve this, Landsat satellite images spanning the period from 1984 to 2021 were processed and analyzed in a ten-year time series. Sixty land points were sampled, including thirty points from forested areas and thirty points from pasture and treeless regions. The normalized vegetation cover index was employed to assess the extent of deforestation and its associated impact on the region. The surface temperature of the study area was determined using the single-channel method. Subsequently, a control region was selected to mitigate the impact of global warming, allowing for a statistical comparison between the study region and the control region. The classification results based on areas with trees and non-trees revealed that approximately 1416 hectares of forested land were deforested from 1984 to 2021. The density of trees in the region decreased from 0.861 percent to 0.816 percent over this period. Additionally, the calculation of surface temperature demonstrated an upward trend of approximately 0.847 degrees Celsius in the study area during the same time frame. The results of the final Welch T-test revealed a significant difference between the temperatures of the two regions at a 99% confidence level, with a p-value of 0.0007. This finding indicates the significant impact of deforestation on the temperature increase in the region. By selecting the control area to mitigate the influence of global temperature increase, the obtained probability value further emphasizes the strong effect of deforestation on the rise in temperature stress in the studied area.

References

Ahamed, T., Tian, L., Zhang, Y., & Ting, K. C. (2011). A review of remote sensing methods for biomass feedstock production. *Biomass and bioenergy*, 35(7), 2455-2469.

Alavi-Panah, Seyyed Kazem. 2008: Thermal remote sensing. Tehran University Printing and Publishing Institute. Sixth edition. 666 p.

Alrababah, M. A., & Alhamad, M. N. (2006). Land use/cover classification of arid and semi‐ arid Mediterranean landscapes using Landsat ETM. *International journal of remote sensing*, 27(13), 2703-2718.

Behzadi, S., & Mousavi, Z. (2019). A novel agent-based model for forest fire prediction. *Earth Observation and Geomatics Engineering*, 3(2), 51-63. doi: 10.22059/eoge.2020.283932.1051

Bruvoll, A., Fæhn, T., & Strøm, B. (2003). Quantifying central hypotheses on environmental Kuznets curves for a rich economy: A computable general equilibrium study. *Scottish Journal of Political Economy*, 50(2), 149-173.

Chen, D., Yu, M., González, G., Zou, X., & Gao, Q. (2017). Climate Impacts on Soil Carbon Processes along an Elevation Gradient in the Tropical Luquillo Experimental Forest. *Forests*, 8(3), 90. doi:10.3390/f8030090

Cinoğlu, D., Epstein, H. E., Tepley, A. J., Anderson-Teixeira, K. J., Thompson, J. R., & Perakis, S. S. (2021). Climatic Aridity Shapes Post-Fire Interactions between Ceanothus spp. and Douglas-Fir (Pseudotsuga menziesii) across the Klamath Mountains. *Forests*, 12(11), 1567.

Cristóbal, J., Jiménez-Muñoz, J. C., Prakash, A., Mattar, C., Skoković, D., & Sobrino, J. A. (2018). An improved single-channel method to retrieve land surface temperature from the Landsat-8 thermal band. *Remote Sensing*, 10(3), 431.

De Frenne, P., Lenoir, J., Luoto, M., Scheffers, B. R., Zellweger, F., Aalto, J., ... & Hylander, K. (2021). Forest microclimates and climate change: Importance, drivers and future research agenda. *Global Change Biology*, 27(11), 2279-2297.

Derrick, B., Ruck, A., Toher, D., & White, P. (2018). Tests for equality of variances between two samples containing both paired and independent observations. *Journal of Applied Quantitative Methods*, 13(2), 36-47.

Dobson, A. P., Bradshaw, A. D., & Baker, A. J. (1997). Hopes for the future: restoration ecology and conservation biology. *Science*, 277(5325), 515-522.

Feizizadeh, B., Hassanitabar, S. M., & Jafarzadeh, J. (2018). Evaluating applying image fusion and optimizing techniques for improving the scale parameter of segmentation in object-based image analysis approach. *Geography and Planning*, 22(65), 223-241.

Gates, David M. (1980). Biophysical Ecology, Springer-Verlag, New York, 611 p.

Ghanbari, F., & Shataee, S. (2010). Investigation of forest extends changes using aerial photos and ASTER imagery (Case study: Border forests in south and southwest of Gorgan city).

Hashemi, S., Fatemi Talab, S., Kavousi Kalashmi, H., Madanipour Kermanshahi, M. (2016). Change detection in the forest cover of Siyahmezgi watershed of Guilan using LandSat images. *Journal of RS and GIS for Natural Resources*, 7(3), 78-88.

He, T., Shao, Q., Cao, W., Huang, L., & Liu, L. (2015). Satellite-observed energy budget change of deforestation in northeastern China and its climate implications. *Remote Sensing, 7*(9), 11586-11601.

Higginbottom, T. P., Collar, N. J., Symeonakis, E., & Marsden, S. J. (2019). Deforestation dynamics in an endemic-rich mountain system: Conservation successes and challenges in West Java 1990–2015. *Biological Conservation, 229*, 152-159.

Hofmeister, J., Hošek, J., Brabec, M., Střalková, R., Mýlová, P., Bouda, M., ... & Svoboda, M. (2019). Microclimate edge effect in small fragments of temperate forests in the context of climate change. *Forest Ecology and Management, 448*, 48-56.

Imani, B., Sattari, F., & Jafarzadeh, J. (2020). Evaluating metropolises grow and their impact on the around villages using Object-Oriented Images Analysis method by using Sentinel-2 & Landsat data. *TeMA-Journal of Land Use, Mobility and Environment, 13*(1), 41-53.

Isaya Ndossi, M., & Avdan, U. (2016). Application of open source coding technologies in the production of land surface temperature (LST) maps from Landsat: A PyQGIS plugin. *Remote sensing, 8*(5), 413.

Jafarzadeh, J. (2022). Investigating the impact of the geothermal power plant on the vegetation around the site using satellite image processing, case study: Meshkinshahr Geothermal Power Plant. *Journal of Remote Sensing and Geographical Information System in Environmental Sciences, 2*(4), 117-101. doi: 10.22034/rsgi.2023.15840

Jafarzadeh, J., & Attarchi, S. (2023). Increasing the Spatial Accuracy of the Land Use Map Using Fusion of Optical and Radar Images of Sentinel and Google Earth Engine. *ISPRS Annals of Photogrammetry, Remote Sensing and Spatial Information Sciences, 14*, 321-326.

Jafarzadeh, J., & Nazmfar, H. (2019). Classification of Satellite Images in the Evaluation of Urban Land Use Change Using Scale Optimization in Objected Oriented Processing (Case Study: Ardabil City).

Jafarzadeh, J., Kakroodi, A. A., & Erfanifard, Y. (2023). Investigating the Impact of Deforestation on Microclimate and Increasing the Risk of Heat Stress Using Satellite Image Processing (case Study: Forests of Hiran Area). *ISPRS Annals of Photogrammetry, Remote Sensing and Spatial Information Sciences, 14*, 315-320.

Jafarzadeh, J & Hasanitabar, SM. (2021). The use of thermal remote sensing in extracting the temperature of the earth's surface and checking its compliance with land use patterns. *Journal of Remote Sensing and Geographical Information System in Environmental Sciences, 1*(1), 51-66.

Kim, O. S. (2010). An assessment of deforestation models for reducing emissions from deforestation and forest degradation (REDD). *Transactions in GIS, 14*(5), 631-654.

Liu, L., & Zhang, Y. (2011). Urban heat island analysis using the Landsat TM data and ASTER data: A case study in Hong Kong. *Remote sensing, 3*(7), 1535-1552.

Lobo, A., Legendre, P., Rebollar, J. L. G., Carreras, J., & Ninot, J. M. (2004). Land cover classification at a regional scale in Iberia: separability in a multi-temporal and multi-spectral data set of satellite images. *International Journal of Remote Sensing, 25*(1), 205-213.

Mahmoudzadeh, H., & Azizmoradi, M. (2019). Deforestation modeling using artificial neural network and GIS (Case study: forests of Khorramabad environs). *Journal of RS and GIS for Natural Resources, 10*(4), 74-90.

McElduff, F., Cortina-Borja, M., Chan, S. K., & Wade, A. (2010). When t-tests or Wilcoxon-Mann-Whitney tests won't do. *Advances in physiology education, 34*(3), 128-133.

Nasirnia, F., & Esmaeili, A. (2008). Investigation of Deforestation in Iran and Neighboring Countries: Application Kuznets Model. *Agricultural Economics, 3*(10), 17-31.

Nazmfar, H., & Jafarzadeh, J. (2018). Classification of satellite images in assessing urban land use change using scale optimization in object-oriented processes (a case study: Ardabil city, Iran). *Journal of the Indian Society of Remote Sensing, 46*, 1983-1990.

Rongali, G., Keshari, A. K., Gosain, A. K., & Khosa, R. (2018). Split-window algorithm for retrieval of land surface temperature using Landsat 8 thermal infrared data. *Journal of Geovisualization and Spatial Analysis, 2*, 1-19.

Schultz, B. B. (1985). Levene's test for relative variation. *Systematic Zoology, 34*(4), 449-456.

Singh, S., Reddy, C. S., Pasha, S. V., Dutta, K., Saranya, K. R. L., & Satish, K. V. (2017). Modeling the spatial dynamics of deforestation and fragmentation using Multi-Layer Perceptron neural network and landscape fragmentation tool. *Ecological Engineering, 99*, 543-551.

Sodhi, N. S., Koh, L. P., Brook, B. W., & Ng, P. K. (2004). Southeast Asian biodiversity: an impending

disaster. *Trends in ecology & evolution, 19(12),* 654-660.

Stehman, S. V. (2004). *A critical evaluation of the normalized error matrix in map accuracy assessment. Photogrammetric Engineering & Remote Sensing, 70(6), 743-751.*

Vandegriend, A. A., Owe, M., Vugts, H. F., & Ramothwa, G. K. (1992). *Botswana water and surface energy balance research program. Part 1: Integrated approach and field campaign results (No. BCRS-91-38A-PT-1).*

Welch, B. L. (1947). *The generalization of 'STUDENT'S'problem when several different population varlances are involved. Biometrika, 34(1-2), 28-35.*

Ya'acob, N., Azize, A. B. M., Mahmon, N. A., Yusof, A. L., Azmi, N. F., & Mustafa, N. (2014, March). *Temporal forest change detection and forest health assessment using Remote Sensing. In IOP Conference Series: Earth and Environmental Science (Vol. 19, No. 1, p. 012017). IOP Publishing.*

Zeng, Z., Wang, D., Yang, L., Wu, J., Ziegler, A. D., Liu, M., ... & Wood, E. F. (2021). *Deforestation-induced warming over tropical mountain regions regulated by elevation. Nature Geoscience, 14(1), 23-29.*

Zhang, J., Wang, Y., & Li, Y. (2006). *A C++ program for retrieving land surface temperature from the data of Landsat TM/ETM+ band6. Computers & geosciences, 32(10), 1796-1805.*

APPENDICES

١- *Specifications of Landsat satellite images used in this research*

Pass	Row	Date	Landsat Scene
١٦٧	٠٣٣	١٩٨٤/٠٨/٢٠	LT٠۵_L١TP_١٦٧٠٣٣_١٩٨٤٠٨٢٠_٢٠١٧٠٢٢٠_٠١_T١
١٦٧	٠٣٣	١٩٩٤/٠۵/٢٨	LT٠۵_L١TP_١٦٧٠٣٣_١٩٩٤٠۵٢٨_٢٠١٨٠٦٠٨_٠١_T١
١٦٧	٠٣٣	٢٠٠۵/٠٦/١١	LT٠۵_L١TP_١٦٧٠٣٣_٢٠٠۵٠٦١١_٢٠٢٠٠٩٠٢_٠٢_T١
١٦٧	٠٣٣	٢٠١٤/٠٧/٢٢	LC٠٨_L١TP_١٦٧٠٣٣_٢٠١٤٠٧٢٢_٢٠١٧٠٤٢١_٠١_T١
١٦٧	٠٣٣	٢٠٢١/٠٦/٢٣	LC٠٨_L١TP_١٦٧٠٣٣_٢٠٢١٠٦٢٣_٢٠٢١٠٦٢٩_٠١_T١